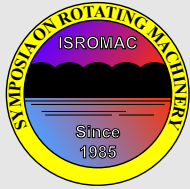


Experimental deposition of NaCl particles from turbulent flows at gas turbine temperatures

Peter Forsyth*, David Gillespie, Matthew McGilvray



ISROMAC 2017

International
Symposium on
Transport Phenomena
and
Dynamics of Rotating
Machinery

Maui, Hawaii

December 16-21, 2017

Abstract

The ingestion and deposition of solid particulates within gas turbine engines has become a very significant concern for both designers and operators in recent times. Frequently aircraft are operated in environments where sand, ash, dust, and salt are present, which can drive damage mechanisms from long term component degradation to in-flight flame-out. Experiments are presented to assess deposition characteristics of sodium chloride (NaCl) at gas turbine secondary air system temperature conditions in horizontal pipe flow. Mono-disperse NaCl particles were generated in the size range 2.0 - 6.5 μm , with gas temperatures 390-480 $^{\circ}\text{C}$, and metal temperatures 355-730 $^{\circ}\text{C}$. Two engine-representative surface roughnesses were assessed. An experimental technique for the measurement of deposited NaCl based on solution conductivity was developed and validated. Experiments were carried out under isothermal and non-isothermal/thermophoretic conditions. An initial experimental campaign was conducted under ambient and isothermal conditions; high temperature isothermal results showed good similarity. Under thermophoretic conditions deposition rates varied by up to several orders of magnitude compared to isothermal rates.

Keywords

Particle deposition — Gas turbine — Turbulent flow — High temperature — Thermophoresis

Department of Engineering Science, University of Oxford, Oxford, United Kingdom

*Corresponding author: peter.forsyth@eng.ox.ac.uk

INTRODUCTION

The deposition of micron-sized particulates from turbulent gas flow has been a subject of investigation for over 60 years. Interest from within the gas turbine community has become very significant over the last 30 years due to numerous threats to engine life. Ingested sand, dust, volcanic ash, salt, and ice crystals can drive various damage mechanisms which can substantially reduce component life [1]. Studies of deposition within secondary air systems studies have shown that significant blockage of film cooling hole can occur for high pressure turbine (HPT) blade conditions [2]. In the main gas path particle effects include fouling and erosion of compressor surfaces, and accretion onto nozzle guide vanes and HPT blades [3, 4].

Computational studies of such geometries have tended to apply standard and widely-available numerical models for the interaction of particles with gas turbulence, including the discrete random walk [5]. These have been shown to be inappropriate for such modelling [6]; to address this the continuous random walk model [7] has been applied to gas turbine flows [8]. This model has been assessed at ambient conditions [9], and now requires validation at engine-representative temperatures.

This paper presents experimental data for assessment of the validity of the continuous random walk model at temperatures and Reynolds numbers representative of conditions in gas turbine secondary air systems. Horizontal pipe flow experiments are reported, using a sodium chloride (NaCl) aerosol. Tests are undertaken with both isothermal and wall-

gas temperature gradient conditions in order to assess thermophoretic effects. Thermophoresis is a particle force due to temperature gradients within the gas phase, proportional to the temperature gradient, in the negative direction. When $T_{\text{gas}} > T_{\text{wall}}$ the rate of deposition observed is increased in comparison to isothermal conditions ('increasing' thermophoresis), for $T_{\text{gas}} < T_{\text{wall}}$ the reverse is observed ('decreasing' thermophoresis). To the authors' knowledge, only one study [10] has addressed decreasing thermophoresis experimentally.

1. BACKGROUND

Deposition is presented in this paper in terms of non-dimensional deposition velocity V_d^+ ,

$$V_d^+ = \frac{J}{C_0 u^*} = \frac{1}{4} \frac{D_h}{L} \frac{U}{u^*} \ln \left(\frac{1}{1 - f_d} \right), \quad (1)$$

and non-dimensional particle relaxation time τ_p^+ ,

$$\tau_p^+ = \frac{C_c \rho_p \rho_f d_p^2 u^{*2}}{18 \mu^2} = Stk \cdot Re \cdot C_f. \quad (2)$$

In the absence of significant body forces except those due to particle-gas relative motion, particle motion can be divided into three regimes, Fig. 1. This shows some of the most widely referenced experimental data, including [11, 12, 13]. These experiments were carried out in vertical pipe flow for particle

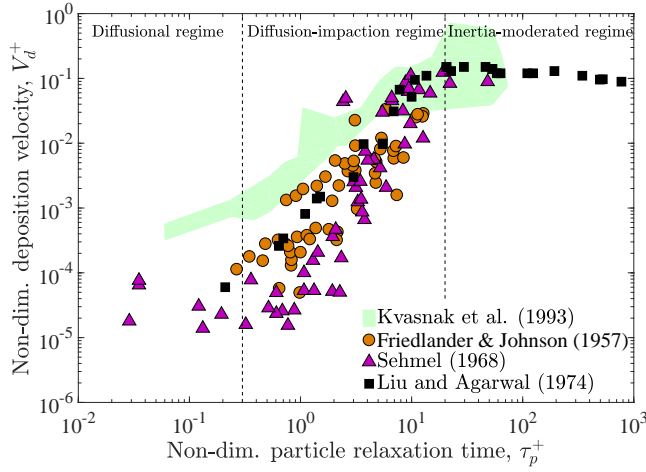


Figure 1. Summary of some key experimental data for particle deposition in turbulent vertical pipe (markers) and horizontal channel (green region) flows at ambient conditions. Adapted from [17].

diameters 0.1-100 μm at Reynolds numbers of 4 000 – 50 000, with a range of particle types, and at ambient temperatures and pressures. The green region indicates the data of Kvasnak et al. [14] who carried out similar experiments in horizontal channel flow. These data, which are representative of other horizontal experiments [15, 16], can be seen to have higher deposition rates in the diffusional and diffusion-impaction regimes, and a reduced dependency of V_d^+ on τ_p^+ .

Based on expected particle sizes (0.5-10 μm) and secondary air systems conditions (T_g, ρ_g, u^*), particle τ_p^+ values are expected to fall into the *diffusion-impaction* and *inertia-moderated* regimes. In the *diffusion-impaction* regime, particles have enough inertia to be effected by turbulent eddies, which can give the particles sufficient wall-normal velocity to deposit onto boundary surfaces. A strong dependence on τ_p^+ is seen. In the *inertia-moderated* regime particle response to turbulence fluctuations decreases as particle inertia becomes too large to be effected by all but the largest eddies.

The majority of particle deposition experiments applicable to gas turbine engines have assessed main gas path geometries [4, 18], using engine(-scale) components at engine-representative temperatures. These studies have shown a significant particle temperature dependency on deposition rate; above an adherence or softening temperature threshold the rate of deposition has been shown to increase very significantly. These findings corroborate a number of studies of deposition in secondary air systems; [1, 2] investigated sand ingestion and blocking of film cooling holes. All reported increased rate of hole blockage with increasing metal temperature above a threshold and varying composition effects.

The more complex geometries undertaken by the above studies make it hard to decouple flow-related and geometry-related effects on deposition. By removing much of the geometric complexity, the experimental results presented here attempt to address the underlying physics of the problem.

2. THERMOPHORETIC PARAMETER

A new thermophoretic parameter is derived below. Initially we take a force balance on an aerosol particle suspended in a gas, giving net acceleration,

$$\frac{d^2 \mathbf{x}}{dt^2} = \mathbf{a}_D + \mathbf{a}_G + \mathbf{a}_{Th}. \quad (3)$$

Note that forces due to Brownian motion and lift are neglected due to large relative particle size and high particle to gas density ratio respectively. Here the drag component of acceleration is given by

$$\mathbf{a}_D = \frac{1}{\tau_p} \frac{C_D Re_p}{24} (\mathbf{U} - \mathbf{V}), \quad (4)$$

where particle Reynolds number Re_p is defined by

$$Re_p = \frac{\rho_g |\mathbf{U} - \mathbf{V}| d_p}{\mu_g}, \quad (5)$$

The drag coefficient is defined by

$$C_D = \frac{24}{Re_p} \quad (6)$$

for $Re_p < 1$, and by

$$C_D = \frac{24}{Re_p} \left(1 + 0.15 Re_p^{0.687} \right), \quad (7)$$

for $1 \leq Re_p < 400$ [19]. The gravitational component \mathbf{a}_G is defined

$$\mathbf{a}_G = \mathbf{g}, \quad (8)$$

as the particle to gas density ratio is so high ($\rho_p/\rho_g \sim 1000$).

The thermophoretic acceleration, \mathbf{a}_{Th} , is experienced by particles proportional to the negative direction of temperature gradient,

$$\mathbf{a}_{Th} = -\Phi \frac{\mu^2 d_p}{\rho_g m_p} \frac{\nabla T_g}{T_g}. \quad (9)$$

Here ∇T_g is the gas temperature gradient and Φ the thermophoretic coefficient ($\Phi = \Phi(\Lambda, Kn)$). The thermal conductivity ratio Λ is defined $\Lambda = k_p/k_g$, where k_p and k_g are the particle and gas (translation component only, $k_g = 15/4\mu R$) thermal conductivities. Knudsen number is defined $Kn = 2l_g/d_p$, where $l_g = \mu\sqrt{\pi/(2P_g\rho_g)}$ is molecular mean free path of the gas, and d_p particle diameter. In the case of hot gas, cool wall, an increase in particle deposition rate is seen ('increasing' thermophoresis). In the reverse case

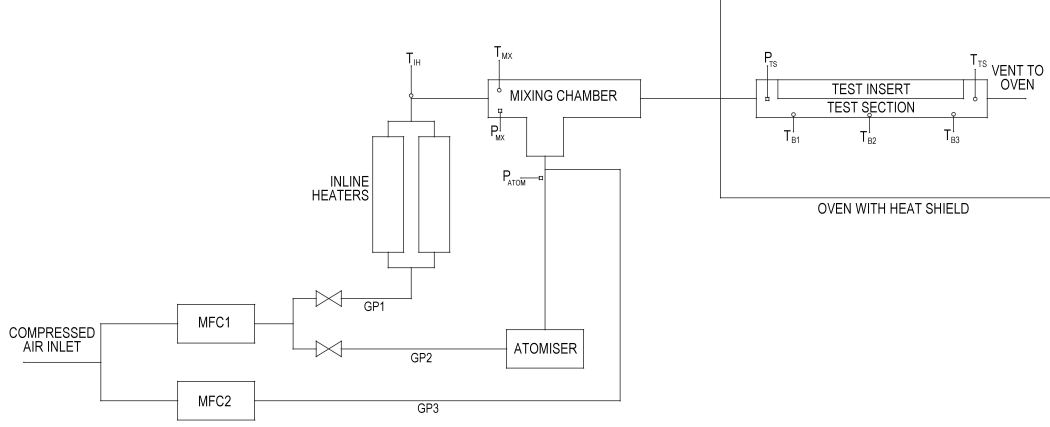


Figure 2. Schematic of experimental rig

with cool gas, hot wall, rate of particle deposition is decreased (‘decreasing’ thermophoresis). A range of expressions exist for the thermophoretic coefficient Φ , summarised in Table 1 of Healy and Young [10]. It has been shown [10, 20, 21] that the expression of Beresnev and Chernyak reproduces the high- Λ behaviour of NaCl particles to a much higher fidelity than the very widely used expression of Talbot [22].

The expression of Beresnev and Chernyak was derived from an analysis based on the S-model, a higher-order linearisation of the Boltzmann equation collision integral than the (more widely used) BGK equation. The thermophoretic coefficient is dependent functions $f_{k,1}$, for $k = 1 - 4$,

$$\Phi = \frac{2\pi}{Kn} \left[\frac{f_{11} + \Lambda f_{21}}{f_{31} + (1 + 2.5\Lambda Kn) f_{41}} \right]. \quad (10)$$

Functions $f_{k,1}$ are tabulated in the original paper for varying R_{BC} ($= \sqrt{\pi}/2Kn$). Use of the expression necessitates interpolation of Φ from the given values of R_{BC} .

We define a normalised thermophoretic parameter P_{th}^+ to attempt to collapse the deposition curves at varying thermophoretic conditions. Starting from the equation for thermophoretic acceleration, Eq. 9, this can be written

$$\mathbf{a}^{Th} = -\Phi \frac{6\mu^2}{\pi\rho_g\rho_p d_p^2} \frac{\nabla T_g}{T_g}, \quad (11)$$

which is non-dimensionalised by $(u^*)^2/d_p$,

$$P_{Th}^+ = \frac{\mathbf{a}^{Th}}{(u^*)^2/d_p} = -\Phi \frac{6\mu^2}{\pi\rho_g\rho_p d_p} \frac{\nabla T_g}{(u^*)^2 T_g}. \quad (12)$$

This can then be expressed in terms of τ_p^+ and the Epstein number, $Ep = d_p \nabla T_g / T_g$,

$$P_{Th}^+ = \frac{-\Phi Ep}{6\pi \tau_p^+}. \quad (13)$$

This is plotted against normalised deposition fraction, \bar{f}_d , the ratio of deposition fraction for non-isothermal to isothermal matched tests. All test conditions (Re , d_p , T_g) are kept constant between the matched isothermal and non-isothermal tests, with the exception of the wall temperature, which is changed,

$$\bar{f}_d = \frac{f_{d, non-isothermal}}{f_{d, isothermal}}, \quad (14)$$

Deposition fraction is calculated from

$$f_d = \frac{m_d}{m_{in}}, \quad (15)$$

where m_d is the measured deposited mass during a test, and m_{in} the the injected mass. For $T_{gas} > T_{wall}$ we expect $\bar{f}_d > 1$; the reverse for $T_{gas} < T_{wall}$. If \bar{f}_d is correlated against P_{Th}^+ , for a given aerosol, the change in deposition fraction with thermophoresis from isothermal conditions can be calculated.

3. METHODS

3.1 Experimental design

An experimental rig was built in a horizontal pipe flow configuration, Fig. 2. Gas was compressed air, pre-dried and supplied by the laboratory 7barg line. Heating of the gas was achieved using inline pipe heaters (Omega AHP-7562 heaters, rated to 540°C, max flow rate 567l/min), gas path 1 (GP1) and a section wrapped in heater tape (Omega Ultra-high temperature heater tape, STH052-100, 783W, rated to 760 °C). Gas path 2 (GP2) passed through the atomiser, carrying the generated particles into the mixing chamber. Gas path 3 (GP3) enabled the atomiser to be bypassed during the heating processes.

Heating of the test piece body was undertaken using a Wild Barfield oven. Flow regulation and measurement was done using a pair of mass flow controllers (FMA-2612A, 0-500 SLPM (MFC1), and FMA-2609A, 0-50 SLPM (MFC2))

and an orifice plate, calibrated using one of the mass flow controllers. Gas velocities ranging 22–33 m/s and Reynolds numbers 6 500 – 10 000 were achieved, corresponding to friction velocities 1.5–2.1 m/s. Gas and metal/wall temperatures up to 480 °C and 730 °C respectively were achieved.

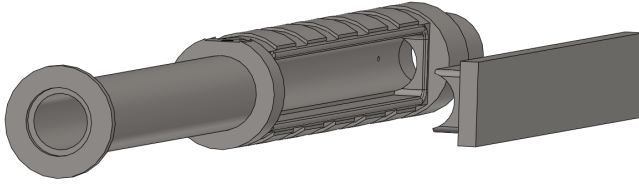


Figure 3. Experimental test piece with test insert removed

The test piece was an 18 mm internal diameter (D_h) bore with a removable test insert, Fig. 3. This allowed measurement of deposited salt aerosol on both the main test piece and test insert by swabbing. The test insert was 160 mm in length, with an included angle of 154°, giving a deposition area of 3878 mm². A $10D_h$ distance existed between mixing chamber and test insert to allow the flow to fully develop. Full rotation about the longitudinal axis was achievable in order to assess gravitational effects. The test insert was clamped into the test piece using an array of six clamps, and sealed using a metal gasket (James Walker, Supagraf Laminated S10).

Two test pieces, EXP α and EXP β , were manufactured from stainless steel grades 304 and 310 respectively. Internal geometries and instrumentation were identical. Surface roughness profiles were measured using a Taylor Hobson surface profilometer, ‘Talysurf’, probe tip diameter 2.5 μ m, and a Gaussian high-pass filter with cut-off wavelength 0.8 mm applied to remove waviness. Roughness is characterised by the arithmetic mean roughness R_a . Calculated surface roughnesses were EXP α : $R_a = 0.22 \mu$ m, EXP β : $R_a = 1.12 \mu$ m. The difference likely occurred due to different post-experiment cleaning methods. Expected engine component finishes of 0.8–1.2 μ m (machined) and $\sim 1.4 \mu$ m (shot peened) indicate that a comparison between deposition on test pieces EXP α and EXP β is relevant to engine conditions.

Instrumentation was in the form of three axial thermocouples measuring test piece body temperature (T_{B1-3}), and a fourth to measure gas temperature 16 mm downstream of end of the test insert (T_{TS}). A pressure tapping in the test piece body wall at the upstream edge of the test insert gave test section static pressure P_{TS} , and could also be used to calculate test section friction velocity (Sensortronics, 0–2 mbar)).

A diverging-straight-converging mixing chamber was designed for the introduction of the particulate laden flow to the heated gas. The mixing chamber was instrumented with a static pressure tapping (P_{MX}), and a thermocouple upstream of the particulate injection (T_{MX}).

3.2 Particle generation

NaCl particles were produced from solution of NaCl (Sigma Aldrich BioXtra, S7653) at ambient temperature and mixed

with the heated flow. Particle diameters 2.0–6.5 μ m were generated, giving non-dimensional particle relaxation times τ_p^+ of 0.7–14.2 at ambient conditions, and 0.4–6.7 at the high temperature conditions. NaCl was chosen due to its close relation to sea salt, with the advantage that its single compound nature allowed simpler measurement of the deposited mass. Its high melting temperature, 801 °C, made possible to use at engine-like conditions, unlike the majority of aerosol particulates generated from solution.

A TSI model 3450 VOAG (vibrating orifice aerosol generator) was used to provide the NaCl particles. The atomiser pumps saline solution through an orifice, which is oscillated using a signal generator and piezoelectric crystal. Tuning of the vibrational frequency to the volumetric flow rate of the solution and droplet diameter can produce mono-disperse droplets. A single droplet is produced per cycle, which are dispersed into a drying column where the solvent evaporates, leaving solid NaCl aerosol particles. The final particle diameter is dependent on solution volumetric concentration of NaCl. Particles are assumed close to spherical as were seen to be circular when viewed under a microscope.

An optical particle sizer (OPS), TSI model 3330, was used to provide both particle size distributions and bulk concentration measurements. The OPS uses a laser scattering/shadow principle to measure optical (rather than aerodynamic equivalent) size. The OPS samples 1.0 l/min air, reporting the size distribution and total count. The total number of particles in the bulk flow is then calculated by multiplying by the actual volume flow rate of the flow from which the sample is drawn. The OPS unit was used to assess the nature of the particle size distribution; distributions with a geometric standard deviations of 1.25 were produced.

3.3 Deposition measurement

A new technique was developed for the measurement of deposited NaCl. The electrical conductivity, measured in S/cm, or more commonly μ S/cm, of a NaCl-water solution is linearly dependent on NaCl concentration; upon dissolving into solution, the Na⁺ and Cl[−] ions disassociate. The internal surfaces of test insert and test section were cleaned repeatedly using a swab, which was rinsed in deionised water. The conductivity of this NaCl-deionised water solution was measured, from which the mass of deposited salt was calculated, based on solution mass and a calibration of solution concentration against conductivity. Solution conductivity is dependent on temperature, which is calibrated to a datum value (25 °C) using temperature compensation coefficient α .

Calibration of the electrical conductivity meter cell constant using standard solutions (potassium chloride, KCl) of known conductivity (Hanna Instruments HI-6033, HI-6031). Manual calibrations of solution concentration against conductivity, temperature compensation coefficient, and swabbing efficiency were carried out. Solution conductivity was indeed seen to be strongly linearly correlated to NaCl concentration across the domain of interest, Fig. 4, with constant of proportionality 0.456 ppm/(μ S/cm), coefficient of determination $r^2 > 0.999$. Two calibrations of α at different solution

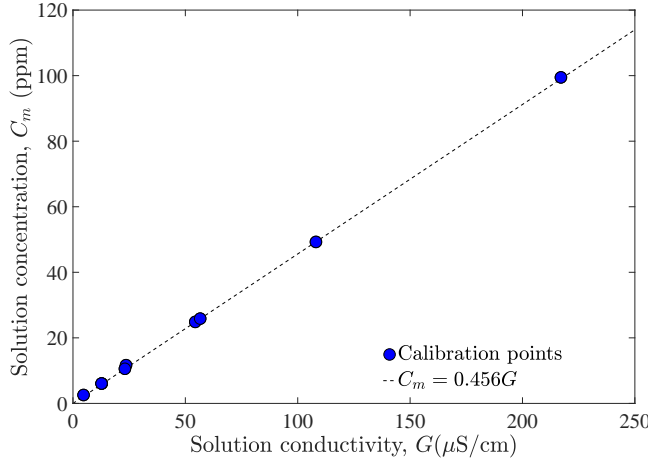


Figure 4. Measured solution conductivity dependence on NaCl concentration. Plotting axis reversed as experimental analysis requires $C_m = C_m(G)$. Conductivity at 25 °C.

concentrations both gave $\alpha = 2.2\%/^{\circ}\text{C}$, with a standard deviations of $0.038\%/^{\circ}\text{C}$ (13 trials) and $0.032\%/^{\circ}\text{C}$ (eight trials). Swabbing efficiency η_s , the ratio of measured fraction to a known deposited mass, was found to have a mean of 0.99, with standard deviation 0.035 (nine trials). A Kern KB-1200-2N balance was used to measure solution mass.

3.4 Experimental uncertainty

A list of uncertainties in the individual measurements taken in each test is given in Table 1. The ‘source’ column indicates the origin of the value: manufacturer-specified (m), manually calibrated (c), assumed (a).

Item	Measurement accuracy/uncertainty	Source
d_p	$\pm 5\%$ mean bin size ¹	m
f_a	$\pm 0.01\%$ reading	c
G	$\pm 1\%$ reading	m/c
\dot{m}_{mfc}	$\pm 1\%$ full scale	m
\dot{m}_{op}	$\pm 5\%$ reading	c
m_{ws}	± 0.01 g	m
P	$\pm 2\%$ reading	c
\dot{Q}_{sol}	$\pm 1\%$	c
T_g, T_w	$\pm 2^{\circ}\text{C}$	m
t	± 1 s	a
η_c	7.2%	c
η_s	3.5%	c

Table 1. Individual accuracies/uncertainties in experimentally measured values. ‘Source’ indicates origin of value; m: manufacturer-specified, c: calibrated, a: assumed.

The Taylor series expansion method of Kline and McKlintock [23] for single-sample uncertainty analysis was used to calculate overall relative uncertainty,

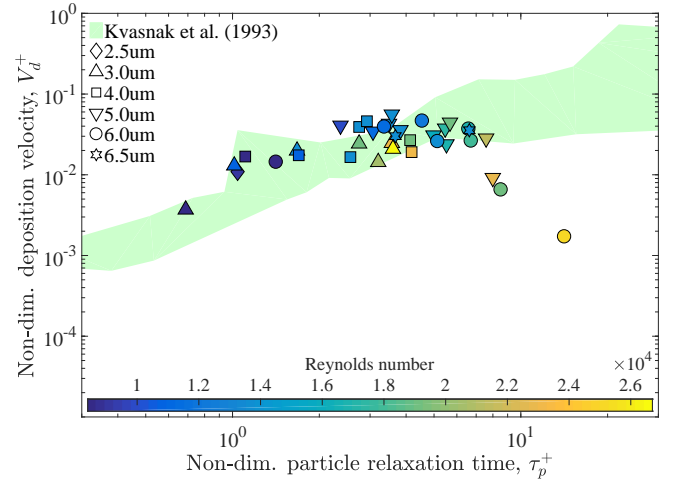


Figure 5. V_d^+ against τ_p^+ for all ambient temperature tests, coloured by Re .

$$\left(\frac{U_R}{R}\right)^2 = \left(\frac{X_1}{R} \frac{\partial R}{\partial X_1}\right)^2 \left(\frac{U_{X1}}{X_1}\right)^2 + \left(\frac{X_2}{R} \frac{\partial R}{\partial X_2}\right)^2 \left(\frac{U_{X2}}{X_2}\right)^2 + \dots + \left(\frac{X_i}{R} \frac{\partial R}{\partial X_i}\right)^2 \left(\frac{U_{Xi}}{X_i}\right)^2, \quad (16)$$

where U_{Xi}/X_i is the relative uncertainty in variable X_i , and $(X_i/R) \partial R / \partial X_i$ the uncertainty magnification factor. For V_d^+ and τ_p^+ , this leads to total uncertainties of 9.9% and 10.4% respectively.

4. RESULTS AND DISCUSSION

4.1 Ambient temperature experiments

A number of ambient temperature tests were carried out to demonstrate the experiment was operating in a comparable manner to other published data, and to investigate the effects of d_p , Re , and surface roughness R_a on deposition rate. The experimental conditions are summarised in Table 2.

Reynolds number, Re	8000-27000
Mean velocity, U (m/s)	7.1-22.9
Friction velocity, U^* (m/s)	0.46-1.27
Temperature, T_g, T_w (°C)	20-22
Nominal particle size, d_p (μm)	2.5-6.5
Non-dim particle relaxation time, τ_p^+	0.7-14.1

Table 2. Operating conditions for ambient temperature experiments.

The experimental data are plotted by particle diameter and bulk Reynolds number in Fig. 5. The green region repre-

¹OPS bins particles by size. Bin width varies based on particle size. We used the mean bin particle diameters for this study: 1.7, 2.0, 2.5, 3.0, 3.7, 4.5, 5.5, 6.8 μm.

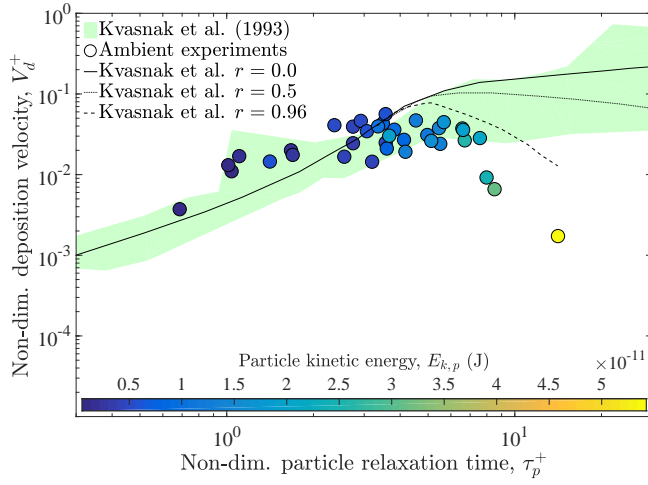


Figure 6. V_d^+ against τ_p^+ for all ambient temperature tests, coloured by nominal particle kinetic energy $E_{k,p}$. Lines show theoretical deposition curves for coefficient of restitution $r = 0.0$, $r = 0.5$, $r = 0.96$ from [14].

sent the data of Kvasnak et al. [14], who carried out deposition experiments in a horizontal channel flow configuration at ambient conditions, with a measurement surface made ‘sticky’ to retain all impacting particles with the application of a thin layer of freon. Regarding the current experiment, some scatter of the data points is seen, though this is almost universally the case with particle deposition experiments, and mostly within the spread of published data.

Two strong trends are seen. For $\tau_p^+ \leq 8$ the experimental data follow the Kvasnak et al. data closely; V_d^+ increasing with τ_p^+ . However for $\tau_p^+ > 8$, V_d^+ is seen to decrease with increasing τ_p^+ , falling 1.5-2 orders of magnitude below what would be expected based on other published data.

The trend of decreasing deposition at higher τ_p^+ is different to the vast majority of published experimental deposition data where V_d^+ is usually seen to increase with τ_p^+ for $0.1 < \tau_p^+ < 50$. It is thought that some particles in this τ_p^+ region are not depositing upon impact. Similar trends have been reported in the literature [24, 14] for high Reynolds number or high friction velocity cases. In the case of our experiments, the rebound or removal is likely due to having dry NaCl particles impacting a dry stainless steel surface, rather than the ‘sticky’ walls favoured by many experimentalists (for example double-sided tape [11], petroleum and glycerine jellies [24], and freon tetrafluoride [14]).

Fig. 6 shows the same data coloured by nominal particle kinetic energy, $E_{k,p}$. Here nominal particle kinetic energy is calculated $E_{k,p} = 0.5m_p U^2$, assuming particles are travelling close to the gas bulk velocity U at impact. A strong trend is seen of decreasing V_d^+ for $E_k > 10^{-11}$ J, with only a single significant deviation seen from this, point (3.7, 0.032). Along with their experimental data, Kvasnak et al. developed an analytical model for rebound, which is shown for varying coefficient of restitution r on the same figure. It is clear that the tail off of the NaCl data is close to the simulated

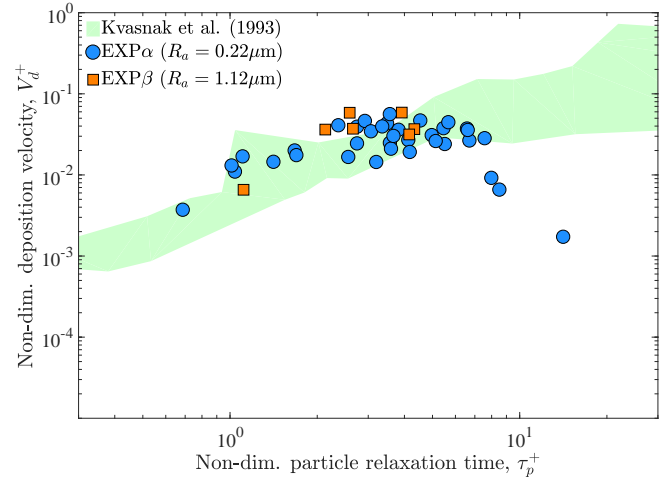


Figure 7. V_d^+ against τ_p^+ for all ambient temperature tests, comparing surface roughnesses. EXP α : $R_a = 0.22 \mu\text{m}$. EXP β : $R_a = 1.12 \mu\text{m}$.

‘ $r = 0.96$ ’ line. Though r is generally seen to vary with impact angle (for example [25]), numerical simulations (as [8]) at $Re = 10\,000$, $26\,000$ and with $d_p = 3, 6 \mu\text{m}$ showed that for both Reynolds numbers $> 90\%$ of impacts occurred at oblique angles below 6° to the wall.

Fig. 7 indicates that surface roughnesses of this magnitude have a noticeable effect on V_d^+ . The EXP β V_d^+ data are generally higher than those for EXP α . For the smallest values of τ_p^+ , a decrease in V_d^+ was seen when the roughness increases. With increasing τ_p^+ , the rougher test piece saw 1.2 – 2.4 \times the deposition of the smoother. Over the seven EXP β tests, the mean increase over EXP α was 1.2 \times .

4.2 High temperature experiments

The high temperature experiments were carried out in the same manner as the ambient temperature campaign, but with gas and metal heated to two temperature conditions representative of the intermediate pressure turbine secondary air system. These are referred to as ‘T1’ (lower gas temperature) and ‘T2’ (higher gas temperature); experimental conditions are outlined in Table 3.

Condition	T1	T2
Re	6 500 – 10 000	7 200
U (m/s)	21.7-33.1	29.5
u^* (m/s)	1.44-2.10	1.93
T_g ($^\circ\text{C}$)	390	480
T_w ($^\circ\text{C}$)	355-630	480-730
d_p (μm)	2.0-6.0	4.0
τ_p^+	0.4-6.7	2.3

Table 3. Operating conditions for high temperature experiments.

The high temperature isothermal data are presented in Fig. 8, and compared to the ambient temperature experiments. It can be seen that the data are very comparable to those at ambient temperatures in general. For $\tau_p^+ > 4$ the hot V_d^+ values are in general lower than the ambient experiments at similar τ_p^+ . A similar tail off appears in V_d^+ for larger τ_p^+ akin with the ambient temperature experiments. As the data are discriminated by d_p and Re it is seen that again this is due to increasing Re . Both the $Re = 10\,000$ data points show this effect, V_d^+ reducing compared to the same particle size at a lower Re .

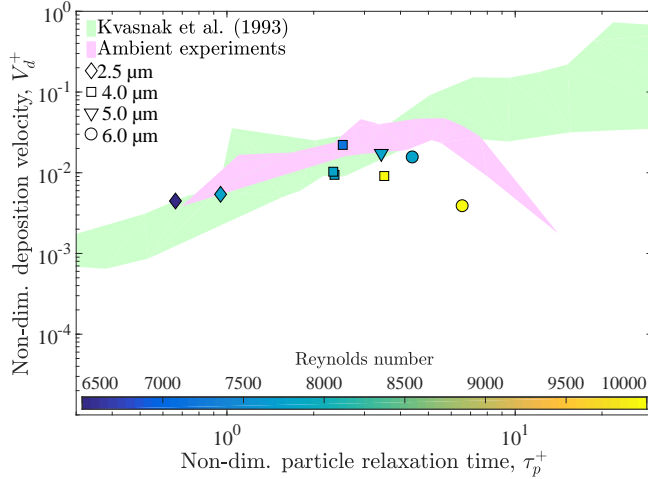


Figure 8. Comparison of all isothermal hot data with ambient temperature experiments.

The two points at $\tau_p^+ = 3.4$ make a useful comparison: $d_p = 4\ \mu\text{m}$, $Re = 10\,000$ (yellow square), and $d_p = 5\ \mu\text{m}$, $Re = 7\,800$ (turquoise triangle). The higher Re case reduces V_d^+ by 46% in comparison to the lower Re case. A number of papers on particle deposition have proposed or accepted Reynolds-independence of V_d^+ , for example Liu and Agarwal [13]. It appears that V_d^+ may not be Re -independent when a dry/non-sticky boundary condition is in place.

Non-isothermal experiments were undertaken with temperature pairings A,B,D,E as outlined in Table 4. Gas temperatures were kept constant for T1 (390 °C), T2 (480 °C) conditions. The majority of experiments were undertaken at T1 conditions, varying τ_p^+ by changing d_p and Re .

Results for the thermophoretic experiments are shown in Fig. 9. Tests T1_A and T1_B were carried out with increasing thermophoresis, $T_g > T_w$, at $Re = 7\,800$. Substantial increases in V_d^+ are seen for only modest gas temperature gradients, relative to the decreasing thermophoretic direction. The T1_B data show fairly constant V_d^+ values across the range of τ_p^+ investigated, with V_d^+ values increasing 1.1–2.5× compared to the isothermal case. At T1_A conditions, stronger thermophoretic conditions are seen to increase V_d^+ 5.5× over isothermal values.

Temperature conditions T1_D and T1_E were undertaken at temperature gradients which gave decreasing thermophoresis. T1_D shows significant reduction in V_d^+ in comparison

Case	T1			T2		
	T_g (°C)	T_w (°C)	P_{Th}^+ $\times 10^{-6}$	T_g (°C)	T_w (°C)	P_{Th}^+ $\times 10^{-6}$
A	390	355	0.68	-	-	-
B	390	383	0.14	-	-	-
C	390	390	0.00	480	480	0.00
D	390	480	-1.9	480	530	-0.92
E	390	630	-5.0	480	730	-6.3

Table 4. Gas and wall temperature pairings A-E for high temperature tests. Indicative P_{Th}^+ values shown for the tabulated gas temperatures with $d_p = 4\ \mu\text{m}$, $Re = 7\,800$ (T1), $Re = 7\,200$ (T2).

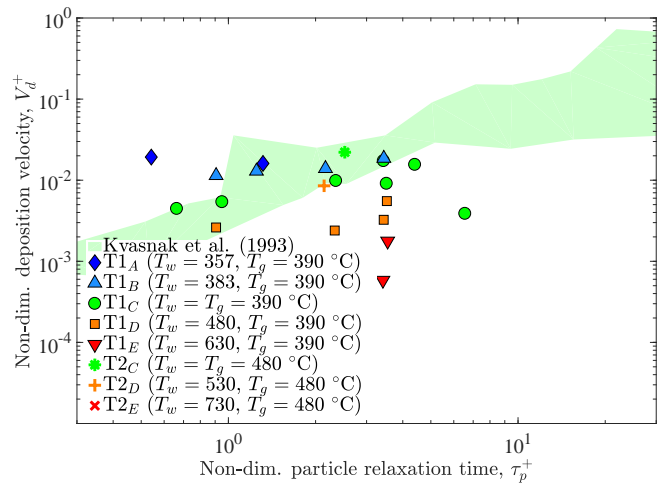


Figure 9. Non-dimensional deposition velocity vs. non-dimensional particle relaxation time for thermophoretic experiments.

to the isothermal data. At low $\tau_p^+ (< 2.5)$, V_d^+ stays fairly constant with τ_p^+ , then increases for $\tau_p^+ > 2.5$, tending back towards the isothermal data line. The effect of varying d_p , Re at constant τ_p^+ indicated a reduction in V_d^+ of 42% between the $d_p = 5\ \mu\text{m}$, $Re = 7\,800$ and $d_p = 4\ \mu\text{m}$, $Re = 10\,000$ cases. This is similar to the reduction at isothermal conditions (46%).

The T1_E experiments used a larger temperature gradient than T1_D; these show a similar trend to the T1_D experiments but of larger magnitude. A larger reduction of 68% between the two varied d_p , Re experiments at constant τ_p^+ is seen for this higher temperature gradient.

The T2 experiments were undertaken at higher gas and wall temperatures than T1. They show a similar trend to T1; although the T2_C (isothermal) and T2_D data points sit higher than the equivalent cruise points, the reduction in deposition fraction is comparable. The T2_E experiment showed extremely low deposition, close to the detection limit of the conductivity meter.

Log of normalised deposition fraction is plotted against thermophoretic parameter P_{Th}^+ for the six thermophoretic

conditions in Fig. 10. Particle thermal conductivity is $k_p = 4.9 \text{ W/m/K}$ for $T_g > 120^\circ\text{C}$. A first order correlation by linear regression is calculated,

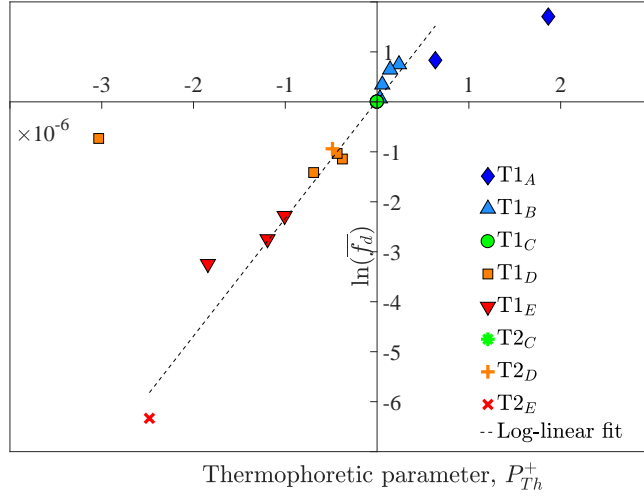


Figure 10. Log of normalised deposition fraction $\ln(\bar{f}_d)$ against thermophoretic parameter P_{Th}^+ .

$$\bar{f}_d = 1.02e^{2.36 \times 10^6 P_{Th}^+}. \quad (17)$$

The linear fit is good for both increasing and decreasing thermophoresis, with more scatter seen for $P_{Th}^+ < -2 \times 10^{-6}$. The scatter is likely due to these points representing experiments undertaken with high, decreasing thermophoresis, where the deposited mass of NaCl was low.

5. CONCLUSIONS AND SUMMARY

A new experimental rig has been built, and an experimental campaign carried out to assess the deposition characteristics of NaCl particles at gas and metal temperatures representative of a gas turbine engine secondary air system. A pipe flow geometry has been utilised to allow comparisons to be made to other existing deposition data at ambient conditions. As the experimental data is for the assessment and validation of numerical models, this geometry is a suitable first step. A method to measure the deposition based on solution electrical conductivity has been developed and validated. Experimental uncertainty has been addressed.

The initial ambient temperature campaign demonstrated that for $\tau_p^+ < 8$, V_d^+ behaves as would be expected in comparison to other ambient measurements. For $\tau_p^+ > 8$ a reduction in V_d^+ is seen. This is thought to be related to some particles rebounding or being removed upon impact, and is noted mainly for the highest nominal particle kinetic energy cases. Due to the experimental set-up we were not able to assess this effect further during the test campaign. A study where NaCl particles were impacted at known angles onto a plate, and the rebound characteristics measured (for example [25]), could be carried out to investigate this effect. The effects of

two engine-representative roughnesses on deposition were assessed; increasing surface roughness at this scale ($R_a < d_p$) was seen to increase deposition by a mean of 1.2×.

At high temperatures, the isothermal tests showed similar trends to those at ambient conditions; at low τ_p^+ the values are well-matched, with a similar tail-off of V_d^+ occurring for $\tau_p^+ > 4$. Both thermophoretic directions (increasing and decreasing deposition) are observed; for $T_{gas} < T_{wall}$ very substantial reductions are seen in deposition velocity. The development of a thermophoretic parameter showed that for there existed a linear relationship between $\ln(\bar{f}_d)$ and P_{Th}^+ for the majority of the experimental data. These provide a large data set for assessment of models for particle - turbulence interaction in numerical simulations.

NOMENCLATURE

Latin

A	Area (m^2)
a	Particle acceleration (m/s^2)
C_0	Mean bulk aerosol concentration (kg/m^3)
C_f	Friction factor ($\frac{\tau_w}{\frac{1}{2}\rho_g U^2}$)
C_m	Solution concentration by mass (ppm)
D_h	Flow hydraulic diameter (m)
d	Particle diameter (m)
$E_{k,p}$	Particle kinetic energy (J)
f_a	Atomiser frequency (Hz)
f_d	Deposition fraction (-)
\bar{f}_d	Normalised deposition fraction (-)
$f_{k,1}$	Functions for calculation of Φ
G	Solution conductivity ($\mu\text{S/cm}$)
g	Gravitational acceleration (m/s^2)
J	Particle wall flux ($\text{kg/m}^2/\text{s}$)
Kn	Knudsen number ($2l_g/d_p$)
k	Thermal conductivity (W/m/K)
L	Length (m)
l_g	gas mean free path (m)
m	Mass (kg)
\dot{m}	Mass flow rate (kg/s)
P	Pressure (Pa)
P_{Th}^+	Thermophoretic parameter
\dot{Q}_g	Bulk gas volume flow (m^3/s)
\dot{Q}_{sol}	Saline solution volume flow rate (m^3/s)
R_{BC}	Beresnev and Chernyak parameter (-)
R	Specific gas constant (J/kg/K)
R_a	Arithmetic mean surface roughness (μm)
Re	Reynolds number ($\frac{\rho_f U D}{\mu}$)

r	Coefficient of restitution
Stk	Stokes number ($\frac{\tau_p}{U/D}$)
T	Temperature (K)
U	Mean flow velocity (m/s)
U_R/R	Relative uncertainty in function R
u^*	Friction velocity ($\sqrt{\frac{\tau_w}{\rho_f}}$) (m/s)
V	Particle velocity (m/s)
V_d^+	Non-dimensional deposition velocity
X_i	Dependent variables of function R
\mathbf{x}	Particle position (m)

Greek

α	Temperature compensation coefficient (%/°C)
η_c	OPS count efficiency (-)
η_s	Swabbing efficiency (-)
Λ	Thermal conductivity ratio
μ	Kinematic viscosity (Pa.s)
ρ	Density (kg/m ³)
τ_p	Particle relaxation time (s) ($\frac{C_c \rho_p \rho_f d_p^2}{18\mu}$)
τ_p^+	Non-dimensional particle relaxation time
τ_w	Wall shear stress (Pa)

Subscripts/Superscripts

amb	Ambient
b	Test piece body
d	Deposition
g	Gas
in	Injected
iso	Isothermal
p	Particle
sol	Solution
ts	Test section
w	Wall
ws	Washing solution
$+$	Non-dimensional form

Abbreviations

EXP α	Experimental test piece A
EXP β	Experimental test piece B
HPT	High pressure turbine
IH	Inline heater
MFC	Mass flow controller
MX	Mixing chamber

OP	Orifice plate
OPS	Optical particle sizer
PSD	Particle size distribution
ppm	Parts per million
SLPM	Standard litres per minute
TI	Test insert
TP	Test piece
VOAG	Vibrating orifice aerosol generator

ACKNOWLEDGEMENTS

The support of Rolls-Royce UK is gratefully acknowledged.

REFERENCES

- [1] N.D. Cardwell, K.A. Thole, and S.W. Burd. Investigation of sand blocking within impingement and film-cooling holes. *Journal of Turbomachinery*, 132:021020–1/10, 2010.
- [2] S. Wylie, A. Bucknell, P.R. Forsyth, M. McGilvray, and D.R.H. Gillespie. Reduction in flow parameter resulting from volcanic ash deposition in engine-representative cooling passages. *Journal of Turbomachinery*, 139(3):031008–13, 2017.
- [3] A. Suman, R. Kurz, N. Aldi, M. Morini, K. Brun, M. Pinelli, and P. Spina. Quantitative CFD analyses of particle deposition on a subsonic axial compressor blade: Part I: particle zones impact. *Journal of Turbomachinery*, 137(2):021009–021009–14, 2014.
- [4] R. Prenter, A. Ameri, and J.P. Bons. Deposition of a cooled nozzle guide vane with nonuniform inlet temperatures. *Journal of Turbomachinery*, 138:101005–1/11, 2016.
- [5] A.D. Gosman and E. Ionnides. Aspects of computer simulation of liquid-fuelled combustors. *Journal of Energy*, 7(6):482–490, 1983.
- [6] L. Tian and G. Ahmadi. Particle deposition in turbulent duct flows - comparisons of different model predictions. *Journal of Aerosol Science*, 38(4):377–397, 2006.
- [7] A. Dehbi. Turbulent particle dispersion in arbitrary wall-bounded geometries: A coupled CFD-Langevin-equation based approach. *International Journal of Multiphase Flow*, 34(9):819–828, 2008.
- [8] P.R. Forsyth, D.R.H. Gillespie, and M. McGilvray. Validation and assessment of the continuous random walk model for particle deposition in gas turbine engines, GT2016-57332. *ASME Turbo Expo*, 2016.
- [9] A. Dehbi. Validation against DNS statistics of the normalized langevin model for particle transport in turbulent channel flows. *Powder Technology*, 200(1):60–68, 2010.
- [10] D.P. Healy and J.N. Young. An experimental and theoretical study of particle deposition due to thermophoresis and turbulence in an annular flow. *International Journal of Multiphase Flow*, 36(11):870–881, 2010.

- [11] S.K. Friedlander and H.F. Johnstone. Deposition of suspended particles from turbulent gas streams. *Industrial and Engineering Chemistry*, 49(7):1151–1156, 1957.
- [12] G.A. Sehmel. Aerosol deposition from turbulent airstreams in vertical conduits. *AEC Research and Development Report*, 1968.
- [13] B.Y.H. Liu and J.K. Agarwal. Experimental observation of aerosol deposition in turbulent flow. *Journal of Aerosol Science*, 5(2):145–155, 1974.
- [14] W. Kvasnak, G. Ahamadi, R. Bayer, and M. Gaynes. Experimental investigation of dust particle deposition in a turbulent channel flow. *Journal of Aerosol Science*, 34(6):795–815, 1993.
- [15] T.L. Montgomery and M. Corn. Aerosol deposition in a pipe with turbulent airflow. *Aerosol Science*, 1(3):185–213, 1970.
- [16] M.R. Sippola and W.W. Nazaroff. Experiments measuring particle deposition from fully developed turbulent flow in ventilation ducts. *Aerosol Science and Technology*, 38(9):914–925, 2004.
- [17] J. Young and A. Leeming. A theory of particle deposition in turbulent pipe flow. *Journal of Fluid Mechanics*, 340:129–159, 1997.
- [18] R. Lundgreen, C. Sacco, R. Prenter, and J.P. Bons. Temperature effects on nozzle guide vane deposition in a new turbine cascade rig, GT2016-57560. *ASME Turbo Expo*, 2016.
- [19] L. Schiller and A. Naumann. A drag coefficient correlation. *Zeitschrift des Vereins Deutscher Ingenieure*, 77:318–320, 1935.
- [20] J.B. Young. Thermophoresis of a spherical particle: Re-assessment, clarification, and new analysis. *Aerosol Science and Technology*, 45(8):927–948, 2011.
- [21] B. Sagot. Thermophoresis for spherical particles. *Journal of Aerosol Science*, 65(1):10–20, 2013.
- [22] L. Talbot, R.K. Cheng, R.W. Schefer, and D.R. Willis. Thermophoresis of particles in a heated boundary layer. *Journal of Fluid Mechanics*, 101(4):737–758, 1980.
- [23] S. J. Kline and F.A. McClintock. Describing uncertainties in single-sample experiments. *Mechanical Engineering*, 75(1):3–8, 1953.
- [24] G.A. Sehmel. Particle eddy diffusivities and deposition velocities for isothermal flow and smooth surfaces. *Aerosol Science*, 4(1):125–138, 1972.
- [25] C.J. Reagle, J.M. Delimont, W.F. Ng, and S.V. Ekkad. Study of microparticle rebound characteristics under high temperature conditions. *Journal of Engineering for Gas Turbines and Power*, 136(1):11501–1/7, 2014.